Sensorless Control of Synchronous Machine With an Inverter Integrated Rotor

Sehwa Choe, *Student Member, IEEE*, Eunsoo Jung, *Student Member, IEEE*, and Seung-Ki Sul, *Fellow, IEEE*

***Abstract*—This paper proposes a new sensorless method for a synchronous machine with an inverter integrated rotor (SMIIR). The SMIIR is a newly developed machine based on the wound rotor synchronous machine (WRSM) but has no brushes and slip-rings. The conventional high-frequency signal injection sensorless methods are based on a physical magnetic saliency. Therefore, the conventional methods cannot be applied to the SMIIR since it has no adequate physical magnetic saliency. The proposed sensorless method suggests a virtual resistance saliency created by the rotor-side inverter, of which the saliency ratio and axes can be arbitrarily set. Based on this virtual saliency, the rotor position information can be included in the relationship between the high-frequency stator voltage and stator current independent of the machine parameters or operating conditions. Because the SMIIR inherently injects a high-frequency voltage for the power transfer, there is no need to inject additional voltage for the proposed high-frequency sensorless control. The initial *d*-axis detection algorithm using the rotor-side inverter without magnetic saturation is also proposed. The feasibility of the proposed sensorless method was verified by the experimental results of the prototype SMIIR.**

***Index Terms*—AC machine, brushless rotating machines, motor drives, sensorless control, signal injection.**

I. Introduction

THE rotor flux position is necessary to perform the vector control of the ac machine [1]. However, the position sensors such as an encoder or a resolver increase the cost and volume of the machine and have reliability issues related to the sensor itself or its associated hardware. Therefore, the so-called position sensorless control methods for finding the rotor flux position without utilizing a position sensor have been researched for over 30 years [2], [3]. These methods are generally classified into two groups according to the principles on which the rotor flux position information is extracted. The first group is based on the back electromotive force (EMF) [4]–[6], and the other group is based on the electrical saliency of the machine [7]–[24].

The second group estimates the rotor flux position through the relationship between the high-frequency stator voltage and current based on the saliency. There are several types of methods in the second group. Some portions of the second group use the pulsewidth modulation current ripple [7]–[10] or a discontinuous signal [11], whereas others not in these portions use a high-frequency signal [12]–[24]. These high-frequency signal injection sensorless methods have two injection algorithms: the rotating voltage signal injection in the stationary reference frame [12]–[14] and the pulsating voltage signal injection in the rotor reference frame [15]–[24]. Because these methods cannot distinguish the magnetic polarity, other methods to detect the magnetic polarity at initial states based on the magnetic saturation have been developed [22], [23].

Most of these methods in the second group are based on the inherent magnetic saliency of the rotor. Even if a machine has no adequate inherent magnetic saliency, a high-frequency sensorless control might be applied based on the induced magnetic saliency [23]. However, a certain limitation on magnitude or frequency of the injected voltage can make this method inapplicable to many cases, because the induced magnetic saliency is highly dependent on the properties of the injected voltage. There was a research among the second group utilizing the high-frequency resistance saliency due to a high-frequency skin effect, but its application is limited to the small machine where the resistance is comparable to the reactance even at the high frequency [24].

Meanwhile, there have been many studies to develop a new kind of ac machine to reduce the rare-earth materials or even eliminate the permanent magnet itself from the ac machine, since the cost and availability of the rare-earth materials, which are indispensable in manufacturing the permanent magnet, have been uncertain.

One of these studies came up with the synchronous machine with an inverter integrated rotor (SMIIR) [25]. The SMIIR, which is shown in Fig. 1, has both a stator-side inverter and a rotor-side inverter connected to its stator winding and rotor winding, respectively, based on the conventional wound rotor synchronous machine (WRSM). The WRSM is known to have some advantages over the permanent-magnet synchronous machine such as an easy field weakening control capability, but have serious disadvantages such as poor efficiency, poor torque density, and the need for mechanical contact to the rotor field winding for power transfer. Although there are many drawbacks to the WRSM, the WRSM has been recently developed and used for traction application of vehicles [26]. By the integration of the rotor-side inverter inside the rotor, the SMIIR inherits the easy field weakening capability of the WRSM but not the disadvantages related to mechanical contact such as contact loss, wear, and longer axial length.

Manuscript received June 4, 2013; revised September 5, 2013; accepted November 22, 2013. Date of publication December 12, 2013; date of current version July 15, 2014. Paper 2013-IDC-387.R1, presented at the 2013 IEEE Applied Power Electronics Conference and Exposition, Long Beach, CA, USA, March 17–21, and approved for publication in the IEEE TRANSACTIONS ON INDUSTRY APPLICATIONS by the Industrial Drives Committee of the IEEE Industry Applications Society.

S. Choe and S.-K. Sul are with Seoul National University, Seoul 110-744, Korea (e-mail: sehwa@eepel.snu.ac.kr; sulsk@plaza.snu.ac.kr).

E. Jung is with Doosan Infracore, Yongin 448-795, Korea (e-mail: Eunsoo.jung@doosan.com).

Color versions of one or more of the figures in this paper are available online at http://ieeexplore.ieee.org.

Digital Object Identifier 10.1109/TIA.2013.2294995

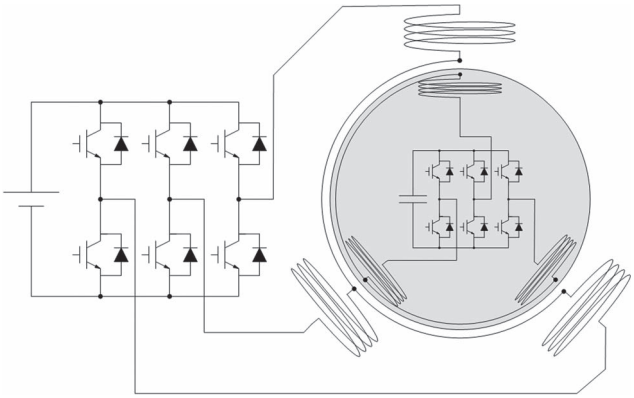

Fig. 1. Structure of the SMIIR.

The SMIIR has power supply issues with the rotor inverter, because there is no mechanical connection between an outside power source and the integrated rotor-side inverter. The rotor-side inverter of SMIIR has to wirelessly receive the power from the stator winding. The power should be equal to the total power loss of the rotor-side circuit, including all losses of the rotor-side inverter and field winding. The detailed operation principles of SMIIR, including power transfer and control, have been described in [25].

In this paper, a signal injection sensorless method for the SMIIR is proposed. The conventional sensorless method based on magnetic saliency cannot be applied to the SMIIR because there is no magnetic saliency due to its round rotor structure.

The proposed method implements a virtual resistance saliency manipulated by the rotor-side inverter. Based on this virtual resistance saliency, the high-frequency signal injection sensorless method can be applied to SMIIR although the machine does not have adequate physical magnetic saliency. This virtual saliency is independent of the physical machine parameter, and therefore, the saliency ratio and axes can be arbitrarily set. The proposed sensorless method uses the inherent high-frequency stator voltage, which is injected to transfer power from the stator-side inverter to the rotor-side inverter in the SMIIR. The voltage is used not only to transfer the power to the rotor-side inverter but also to induce the current response, which contains the rotor position information. Additionally, an initial d-axis detection algorithm without using magnetic saturation is also devised. The feasibility of the proposed method is verified by an experimental test on the prototype SMIIR with an associated control algorithm.

II. Basic Operation Principle of SMIIR

The SMIIR is based on the WRSM, but it has an integrated rotor-side inverter instead of the mechanical contact device such as brushes and slip-rings. The rotor-side inverter consists of a dc link capacitor, switching devices, and its own controller, and it is electrically isolated from the outside of the rotor. The equivalent circuit of the SMIIR in the d-q rotor reference frame can be deduced, as shown in Fig. 2, which is similar to the WRSM or the wound rotor induction machine (WRIM).

The voltage source v^r_{dqs} and v^r_{dqr} denote the output voltages of the stator-side and rotor-side inverters, respectively. i^r_{dqs} and

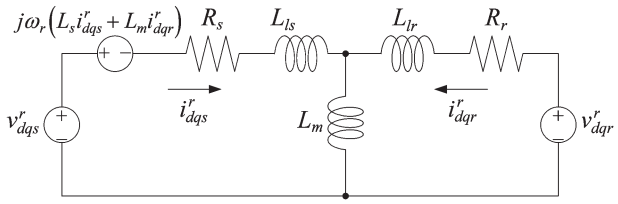

Fig. 2. Equivalent circuit of the SMIIR in the rotor reference d-q frame.

i^r_{dqr} denote the output current of the stator-side and rotor-side inverters, respectively. The inductance and resistance are represented as L and R, respectively. Superscript r denotes that the corresponding variable is expressed in the rotor reference d-q frame; subscripts s, r, l, and m denote that the corresponding variables are related to the stator, the rotor, leakage, and the air gap, respectively; and ω_r denotes the electrical angular frequency of the rotor. The voltage equations of the SMIIR shown in Fig. 2 can be derived as [25]

$$v^r_{dqs} = R_s i^r_{dqs} + \frac{d}{dt}\left(L_s i^r_{dqs} + L_m i^r_{dqr}\right) + j\omega_r\left(L_s i^r_{dqs} + L_m i^r_{dqr}\right) \quad (1)$$

$$v^r_{dqr} = R_r i^r_{dqr} + \frac{d}{dt}\left(L_r i^r_{dqr} + L_m i^r_{dqs}\right) \quad (2)$$

where $L_s = L_m + L_{ls}$, $L_r = L_m + L_{lr}$.

Based on the superposition principle, the control scheme of the SMIIR can be separated into two parts depending on their frequency region. One part uses the fundamental frequency region for the machine drive, including torque control. The other uses the high-frequency region for power transfer to the rotor-side inverter through electromagnetic coupling between the stator winding and rotor winding. The frequency used for the power transfer should be high enough compared with the cutoff frequency of the current controller to avoid interference between power transfer and current regulation. Subscripts f and h denote that corresponding variables are related to fundamental and high-frequency regions, respectively.

The basic operating principle of the SMIIR for torque control remains nearly the same as the WRSM. This means that the rotor-side inverter controls the fundamental frequency component of the d-axis rotor current, i.e., i^r_{drf}, as dc in the rotor reference frame to build a field flux. The stator-side inverter controls the fundamental frequency component of the q-axis stator current, i.e., i^r_{qsf}, to regulate machine torque. In addition, the fundamental frequency components of the q-axis rotor current, i.e., i^r_{qrf}, and the d-axis stator current, i.e., i^r_{dsf}, are regulated as null in the constant torque region to minimize copper losses.

For power transfer from the stator-side inverter to the rotor-side inverter, the stator-side inverter injects the high-frequency stator voltage, i.e., v^r_{dqrh}, and the rotor-side inverter regulates the high-frequency rotor current, i.e., i^r_{dqrh}. The voltage equation of the high-frequency components can be presented in phasor variables as (3) in the steady-state condition and can be approximated as (4), because the high-frequency reactance,

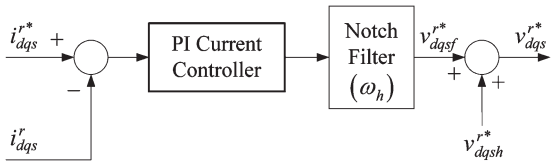

Fig. 3. Structure of the stator-side inverter controller.

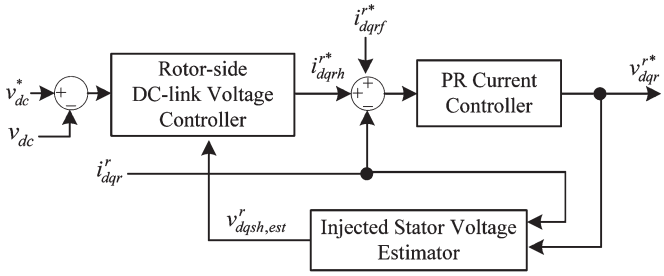

Fig. 4. Structure of the rotor-side inverter controller.

i.e., X_s, is much larger than the stator resistance, i.e., R_s, at the injected high frequency [25]. Thus,

$$\mathbf{V}^r_{dqsh} = (jX_s + R_s)\mathbf{I}^r_{dqsh} + jX_m\mathbf{I}^r_{dqrh} \tag{3}$$

$$\mathbf{V}^r_{dqsh} \approx jX_s\mathbf{I}^r_{dqsh} + jX_m\mathbf{I}^r_{dqrh} \tag{4}$$

where the bold capital letters, i.e., $\mathbf{V}$ and $\mathbf{I}$, mean that the corresponding variables are expressed in phasor at the high-frequency ω_h.

The power transferred through the high-frequency components can be approximated as (5), and therefore, the efficiency of the transferred power is maximized when the phase angle difference between the high-frequency stator voltage, i.e., v^r_{dqsh}, and rotor current, i.e., i^r_{dqrh}, is controlled as π, such as in (6) [25]. Thus,

$$\mathrm{P}_{s,r} \approx -\frac{3}{2}\frac{1}{2}\mathrm{Re}\left(\mathbf{V}^r_{dqsh}\bar{\mathbf{I}}^r_{dqrh}\right) \tag{5}$$

$$\mathbf{I}^r_{dqrh} = -k\mathbf{V}^r_{dqsh} \tag{6}$$

where "$-$" means complex conjugate, and k is a positive control parameter, related to the amount of power transferred to the rotor-side inverter. The value of parameter k depends on the magnitude of the injected stator voltage and the power transferred to keep the dc link voltage of the rotor-side inverter, which means the energy balance of the rotor-side inverter.

The control strategy block diagrams of the stator-side and rotor-side inverters are shown in Figs. 3 and 4, respectively. The stator controller consists of the "PI Current Controller," which regulates the fundamental frequency stator current for the torque control, and cascaded notch filter and the open-loop high-frequency voltage reference for the power transfer. The rotor controller consists of the "Proportional and Resonant (PR) Current Controller" to regulate both fundamental and high-frequency rotor current, and "Injected Stator Voltage Estimator" and "Rotor-side DC-link Voltage Controller" to regulate the energy supply and balance of the rotor-side inverter. A more detailed control scheme can be referenced in [25].

III. Proposed Sensorless Method

In the general sensorless control methods, the accessible data are only the stator voltage reference (or sensed) and sensed stator current. This means that the rotor position information should be extracted from their relationship. In the high-frequency voltage injection sensorless case, the rotor position information can be extracted from the response of the high-frequency stator current, i.e., i_{dqsh}, with regard to the injected high-frequency stator voltage, i.e., v_{dqsh}. However, this extracted rotor position information can be used only when an adequate physical motor saliency exists. Therefore, these conventional methods cannot be applied to the SMIIR, because it does not have sufficient physical saliency.

A. Virtual Resistance Saliency

The SMIIR, which has the rotor-side inverter, can create a virtual saliency. The purpose of the virtual saliency is to imitate the role of the physical saliency, which makes a saliency response of the high-frequency stator current from the injected high-frequency voltage. Because the physical saliency is a characteristic of the passive component, the whole rotor side, including the rotor-side inverter, may be considered as a passive component, not as an active voltage source, for convenience of analysis.

The aim of the virtual saliency can be achieved by proper control of the rotor-side inverter. The rotor-side inverter controls the rotor current directly and can control the stator current indirectly through electromagnetic coupling between the stator and rotor windings. Therefore, it can make the saliency response of the high-frequency stator current, i.e., i_{dqsh}, although there is no physical saliency, by proper control of the high-frequency rotor current, i.e., i_{dqrh}, with regard to the injected high-frequency stator voltage, i.e., v_{dqsh}.

The virtual inductance, whose magnitude is L_{dq}, can be made if the rotor-side inverter synthesizes its output voltage as (7). The minus sign in the rotor current is to make its direction the same as a passive component to apply Ohm's law, i.e.,

$$v^r_{dqrh} = L_{dq}\frac{d\left(-i^r_{dqrh}\right)}{dt}. \tag{7}$$

Thus, the virtual inductance saliency can be achieved by setting the virtual inductance L_{dq} differently as in

$$v^r_{d_{inj}h} = L_{d_{inj}}\frac{d\left(-i^r_{d_{inj}rh}\right)}{dt} \tag{8}$$

$$v^r_{q_{inj}h} = L_{q_{inj}}\frac{d\left(-i^r_{q_{inj}rh}\right)}{dt} \tag{9}$$

where d_{inj} and q_{inj} denote axes where the maximum and minimum values of inductance exist. Because the virtual saliency is independent of the physical saliency, the inductance values and axes of saliency, i.e., d_{inj}- and q_{inj}-axes, can be arbitrarily set and placed.

However, the implementation of this virtual inductance has several problems in the SMIIR. It needs an extra output voltage of the rotor-side inverter whose dc link voltage is quite small

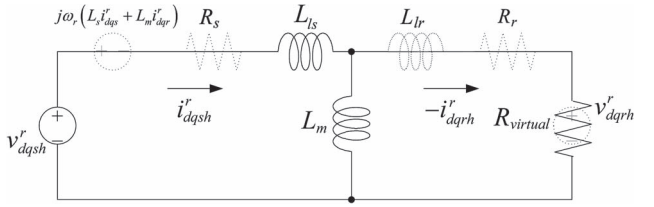

Fig. 5. Equivalent circuit of the SMIIR in the rotor reference d-q frame for the injected high frequency.

to minimize the switching loss of the inverter itself. The extra rotor voltage calls for an increased dc link voltage of the rotor-side inverter and increased losses of the inverter before, finally, increased power transfer from stator inverter.

To avoid these problems, the already existing high-frequency stator voltage, rotor current, and stator current for the power transfer can be simultaneously used for the high-frequency sensorless control. The high-frequency signal injection sensorless method can be applied without additional signals, and therefore, there is no additional loss.

In the first step, the relationship between the high-frequency stator voltage and current is explained as a passive component. In (6), k can be seen as a virtual conductance. In other words, the whole rotor side including the inverter can be seen as a virtual resistance, which is defined as the inverse of a virtual conductance k, as in (10) and as shown in Fig. 5. The minus sign of the rotor current is used to make its direction the same as a passive component. The approximation in (10) is based on the assumption that the air-gap inductance is large compared with the leakage inductance, i.e.,

$$R_{virtual} := \frac{\mathbf{V}^r_{dqrh}}{-\mathbf{I}^r_{dqrh}} \approx \frac{\mathbf{V}^r_{dqsh}}{-\mathbf{I}^r_{dqrh}} = \frac{1}{k}. \tag{10}$$

Similar to the virtual inductance saliency, the virtual resistance saliency can be achieved by setting virtual conductance k differently, as in

$$-\mathbf{I}^r_{d_{inj}rh} = k_{d_{inj}} \mathbf{V}^r_{d_{inj}sh} \tag{11}$$

$$-\mathbf{I}^r_{q_{inj}rh} = k_{q_{inj}} \mathbf{V}^r_{q_{inj}sh} \tag{12}$$

where $k_{d_{inj}}$ and $k_{q_{inj}}$ represent the virtual conductances. The values of these conductances should be set differently to create the virtual saliency.

The virtual saliency is artificially created by the rotor-side inverter, which means that it is not subject to the physical machine parameters. Therefore, the ratio of the virtual conductances can be arbitrarily set, and the axes of saliency can be located at any place away from the physical rotor d- and q-axes. However, the magnitudes of the virtual conductances cannot be arbitrarily set because they are controlled by the "Rotor-side DC link Voltage Controller" in Fig. 4 to balance the rotor-side energy, as mentioned in Section II. Therefore, the virtual resistance saliency can be made only by adjusting the ratio between the maximum and minimum resistance, not by setting their absolute values. The virtual resistance saliency is not affected by operating conditions such as stator and rotor currents, rotating speed, load torque, and temperature as long as the amount of power transferred to the rotor-side inverter remains constant.

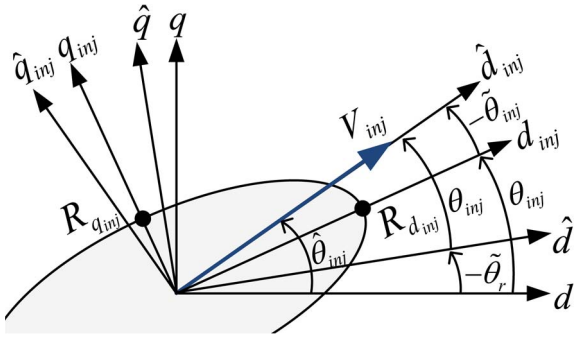

Fig. 6. Diagram of the high-frequency voltage injection scheme.

B. Sensorless Control With the Virtual Resistance Saliency

Based on the virtual resistance saliency, a high-frequency voltage injection sensorless method can be applied. The injection diagram is shown in Fig. 6. The d-axis is where the field flux exists, and the q-axis is its quadratic axis. The d_{inj}- and q_{inj}-axes are where the maximum or minimum virtual resistance, i.e., R_{dinj} or R_{qinj}, is created as (10)–(12). Variable θ_{inj} represents the angle difference between the intended injection axis d_{inj}, where the high-frequency signal is intended to inject, and the rotor d-axis. The symbol "^" denotes that the corresponding variable is an estimated value. For convenience, d_{inj}- and q_{inj}-axes are called the saliency reference frame, and $\hat{d}_{inj}$- and $\hat{q}_{inj}$-axes are called the estimated saliency reference frame.

The high-frequency voltage for the power transfer can be injected along with the estimated injection axis (estimated saliency reference d-axis), i.e., $\hat{d}_{inj}$-axis, as shown in Fig. 6 and in

$$\begin{bmatrix} v^{\hat{r}}_{d_{inj}sh} \\ v^{\hat{r}}_{q_{inj}sh} \end{bmatrix} = V_{inj} \begin{bmatrix} \sin(\omega_h t) \\ 0 \end{bmatrix}. \tag{13}$$

According to the relationship between the saliency reference frame and the estimated saliency reference frame, the injected high-frequency voltage can be expressed in the saliency reference frame as

$$\begin{aligned} \begin{bmatrix} v^r_{d_{inj}sh} \\ v^r_{q_{inj}sh} \end{bmatrix} &= \begin{bmatrix} \cos\tilde{\theta}_r & \sin\tilde{\theta}_r \\ -\sin\tilde{\theta}_r & \cos\tilde{\theta}_r \end{bmatrix} \begin{bmatrix} v^{\hat{r}}_{d_{inj}sh} \\ v^{\hat{r}}_{q_{inj}sh} \end{bmatrix} \\ &= V_{inj} \begin{bmatrix} \cos\tilde{\theta}_r \sin(\omega_h t) \\ -\sin\tilde{\theta}_r \sin(\omega_h t) \end{bmatrix} \end{aligned} \tag{14}$$

where θ means angle, and $\tilde{\theta}_r = \theta_r - \hat{\theta}_r$ denotes the angle error between the rotor d-axis, i.e., d, and the estimated d-axis, i.e., $\hat{d}$. Additionally, angle error $\tilde{\theta}_r$ also coincides with angle difference $\tilde{\theta}_{inj} = \theta_{inj} - \hat{\theta}_{inj}$ between angle θ_{inj} of the intended injection axis, i.e., d_{inj}, and angle $\hat{\theta}_{inj}$ of the estimated injection axis, i.e., $\hat{d}_{inj}$, where the signal is actually injected, as shown in Fig. 6.

Substituting (14) into (11) and (12), the high-frequency rotor current in the saliency reference frame can be calculated as

$$\begin{bmatrix} i^r_{d_{inj}rh} \\ i^r_{q_{inj}rh} \end{bmatrix} = -V_{inj} \begin{bmatrix} k_{d_{inj}} \cos\tilde{\theta}_r \sin(\omega_h t) \\ -k_{q_{inj}} \sin\tilde{\theta}_r \sin(\omega_h t) \end{bmatrix}. \tag{15}$$

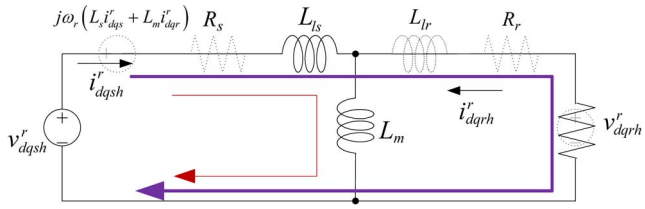

Fig. 7. High-frequency current path.

Substituting (14) and (15) into (4), the high-frequency stator currents in the saliency reference frame can be obtained as

$$\begin{bmatrix} i^r_{d_{inj}sh} \\ i^r_{q_{inj}sh} \end{bmatrix} = -\frac{V_{inj}}{X_s} \times \begin{bmatrix} \sqrt{X_m^2 k_{d_{inj}}^2 + 1}\ \cos\tilde{\theta}_r \sin(\omega_h t + \psi_{d_{inj}}) \\ -\sqrt{X_m^2 k_{q_{inj}}^2 + 1}\ \sin\tilde{\theta}_r \sin(\omega_h t + \psi_{q_{inj}}) \end{bmatrix} \quad (16)$$

where $\psi_{d_{inj}} = \tan^{-1}(1/X_m k_{d_{inj}}) + \pi$ and $\psi_{q_{inj}} = \tan^{-1}(1/X_m k_{q_{inj}}) + \pi$ denote the phase differences between the high-frequency stator voltages and the high-frequency stator currents in saliency reference d- and q-axes, respectively.

In practice, $X_m k_{d_{inj}}$ and $X_m k_{q_{inj}}$ are much larger than unity because the reactance at the injected high frequency is much larger than the corresponding resistances, which are the inverse of the conductances, i.e., $k_{d_{inj}}$ and $k_{q_{inj}}$. Thus, the current path at the high frequency is not through the magnetizing inductance but through the virtual resistance, as shown in Fig. 7. Furthermore, the phase differences $\psi_{d_{inj}}$ and $\psi_{q_{inj}}$ can be approximated to π. In conclusion, the high-frequency stator currents in the estimated saliency reference frame can be derived as in

$$\begin{bmatrix} i^{\hat{r}}_{d_{inj}sh} \\ i^{\hat{r}}_{q_{inj}sh} \end{bmatrix} = \begin{bmatrix} \cos\tilde{\theta}_r & -\sin\tilde{\theta}_r \\ \sin\tilde{\theta}_r & \cos\tilde{\theta}_r \end{bmatrix} \begin{bmatrix} i^r_{d_{inj}sh} \\ i^r_{q_{inj}sh} \end{bmatrix} \approx \frac{X_m V_{inj}}{X_s} \times \begin{bmatrix} k_{d_{inj}} \cos^2\tilde{\theta}_r \sin(\omega_h t) + k_{q_{inj}} \sin^2\tilde{\theta}_r \sin(\omega_h t) \\ \frac{\sin 2\tilde{\theta}_r}{2}(k_{d_{inj}} - k_{q_{inj}}) \sin(\omega_h t) \end{bmatrix}. \quad (17)$$

Because the magnitude of the stator current in the estimated saliency reference q-axis, i.e., $i^{\hat{r}}_{q_{inj}sh}$, is a function of angle error $\tilde{\theta}_r$, angle error information ε_f can be extracted through a simple demodulation process as in

$$\varepsilon_f = LPF\left(i^{\hat{r}}_{q_{inj}sh} \times -\sin\omega_h t\right) \approx -\frac{X_m V_{inj}}{4X_s} \sin 2\tilde{\theta}_r (k_{d_{inj}} - k_{q_{inj}}) \quad (18)$$

where LPF represents a low-pass filtering process to eliminate the $2\omega_h$ frequency component from the signal inside of the parenthesis. Moreover, if the estimated angle error is small enough, (18) can be approximated further into

$$\varepsilon_f \approx -\frac{X_m V_{inj}}{2X_s}(k_{d_{inj}} - k_{q_{inj}})\,\tilde{\theta}_r. \quad (19)$$

Because the virtual resistance saliency can be arbitrarily set, the position error can always be extracted from the high-frequency component of the stator current, regardless of the machine parameters or the operating conditions. Using an appropriate state observer, the rotor position can be identified from the position error information [20]. The proposed sensorless control block diagram is shown in Fig. 8. The speed observer is a classical cascade of PI and integrator, which is also called the "second-order state filter" [13].

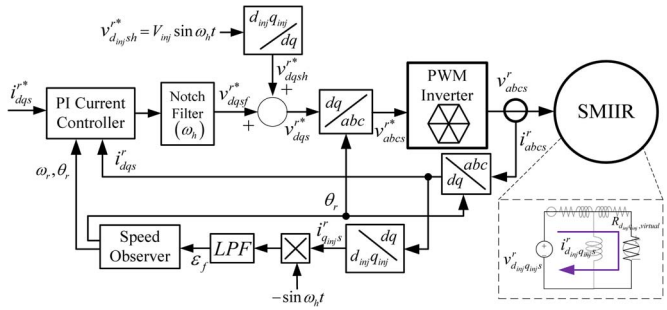

Fig. 8. Control block diagram of the proposed sensorless method.

C. Initial d-Axis Detection

The detection of the d-axis at an initial standstill state is necessary, because the proposed sensorless method can settle down at the $+d$- or $-d$-axes at the initial state similar to the conventional high-frequency sensorless methods. This is because the error information ε_f is a function of two times the angle error $\tilde{\theta}_r$, as seen in (18), which is similar to the conventional methods. The conventional high-frequency signal injection sensorless methods have exploited the asymmetric current responses between the $+d$- and $-d$-axes due to the magnetic saturation related to the rotor flux. However, because the proposed method has limits on the magnitude of the injected voltage, the conventional methods cannot be applicable to the SMIIR.

In contrast to the conventional machine, by exploiting the controllability of the rotor current, the asymmetric current response can be forced by the rotor-side inverter of the SMIIR. Using the asymmetric current response, the polarity of the d-axis can be found. Although the asymmetric current response can be implemented in both the d_{inj}- and q_{inj}-axes, the q_{inj}-axis is only used for the initial polarity detection because the d_{inj}-axis stator current already has a high-frequency signal due to power transfer and sensorless control. Therefore, during the initial angle detection period, the q_{inj}-axis rotor current is regulated by the rotor-side inverter to send a signal to let the stator-side inverter identify whether the estimated initial angle is located on the $+d$-axis or not.

The rotor-side current sent as a signal can be transferred and seen in the stator current by magnetic mutual coupling between the stator and rotor winding. Due to the magnetic mutual coupling, a symmetric ac signal biased with dc is not useful because this signal is not distinguishable in the stator-side viewpoint, as shown in Fig. 9(a), between the $+d$-axis estimation case or the $-d$-axis case. A proper pulse signal can be used to exaggerate the asymmetric response of the signal. If the average of the signal is small enough, the peak signal can be transferred to the stator without severe distortion. If the rotor-side inverter makes $+q_{inj}$-axis peak current and the stator-side inverter senses $+q_{inj}$-axis peak current, then the estimated rotor position is in the $+d$-axis. Otherwise, if the stator-side

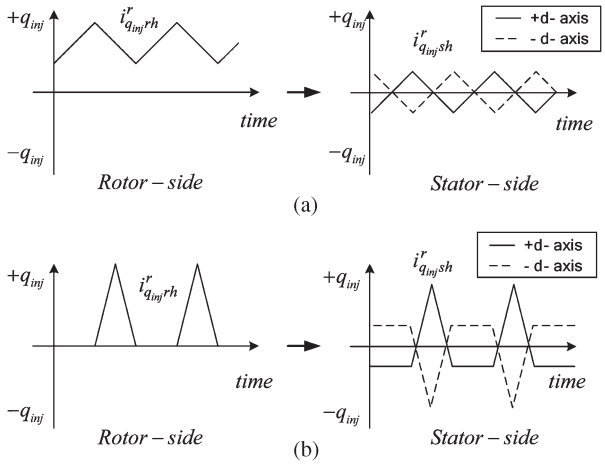

Fig. 9. Current response in the stator according to the polarity of the d-axis. (a) Symmetric ac current with dc bias. (b) Asymmetric ac current with dc bias.

TABLE I
MACHINE PARAMETERS OF THE WRIM MODIFIED TO THE SMIIR

Nominal Parameters	Power	9 [kW]
	Poles	6
	Speed	1165 [r/min]
	Voltage	220 [V_{rms}]
	Stator Current	44 [A_{rms}]
	Rotor Current	29 [A_{rms}]
DC parameter	Rs / Rr	0.112 / 0.09 [Ω]
High-frequency parameter (f_{inj} = 500Hz)	Lls, Llr	0.97 [mH]
	Lm	14.3 [mH]
Control parameter	V_{inj}	25 [V_{peak}]
	$k_{d_{inj}}$ / $k_{q_{inj}}$	0.15 / 0.1 [S]

inverter senses $-q_{inj}$-axis peak current, then the estimated rotor position is in the $-d$-axis, as shown in Fig. 9(b).

According to the equivalent circuit in Fig. 2, the $+q$-axis pulse in the rotor current should be seen as a $-q$-axis pulse in the stator current because the current is set as an output in each inverter. However, in the practical condition, the different phase sequences such as "abc" and "acb" may change the sign of the pulse seen in the stator side. The operation principle of the SMIIR needs only the matched $+d$-axis between the stator side and the rotor side, because rotor-side q-axis current is controlled as null in the fundamental frequency region, and high-frequency rotor-side q-axis current is controlled as a negative to stator voltage as in (11) and (12). In other words, the q-axis current remains the same in the stator-side point of view regardless of the rotor-side phase sequence. Therefore, matching the $+q$-axis between the two inverters is not a concern, and for convenience of explanation, the $+q$-axis rotor current pulse is assumed to be seen as the $+q$-axis stator current pulse.

IV. EXPERIMENTAL RESULTS

To figure out the feasibility of the proposed sensorless method for the SMIIR, experiments have been carried out. The parameters of the test machine are shown in Table I. The test

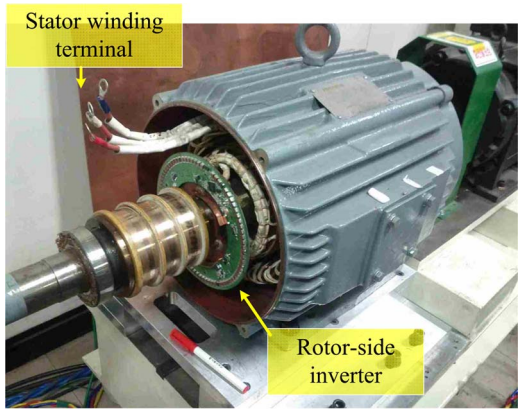

Fig. 10. Experimental test machine: SMIIR.

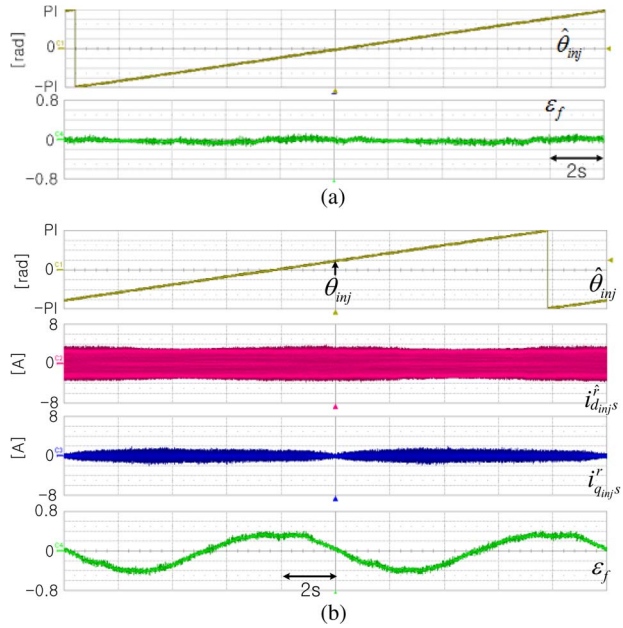

Fig. 11. Experimental results of error information as injection angle changes. (a) Without virtual saliency; original saliency of the SMIIR. (b) With proposed virtual resistance saliency.

machine was modified from an off-the-shelf WRIM where the diameter of the rotor-side inverter is about 20 cm, as shown in Fig. 10. The experimental setup was the same as in Fig. 1 with a load machine. The stator was connected to the outside stator inverter, and the rotor inverter was integrated inside the rotor, as shown in Fig. 10. There was no communication with the integrated rotor-side inverter, including the monitoring of the parameters. That is, only the stator-side inverter was controlled as the typical permanent-magnet synchronous motors. The fundamental frequency region is up to 200 Hz, and the high frequency is 500 Hz.

Fig. 11 shows the experimental results verifying (18). The actual angle of the injected voltage, i.e., $\hat{\theta}_{inj}$, was slowly changed from $-\pi$ to π as the rotor rotated to confirm the electrical saliency. As shown in Fig. 11(a), the SMIIR reveals no physical magnetic saliency for a conventional sensorless control. The waveforms in Fig. 11(b), i.e., $\hat{\theta}_{inj}$, $i^{\hat{r}}_{d_{inj}s}$, $i^{r}_{q_{inj}s}$, and ε_f, clearly reveal the salient responses. In this experiment, the intended injection angle, i.e., θ_{inj}, is set as $\pi/4$ and as

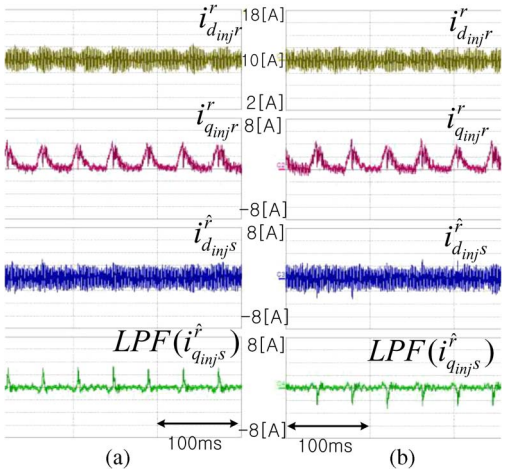

Fig. 12. Experiment results of initial d-axis detection at standstill. (a) Estimated d-axis is aligned to the $+d$-axis. (b) Estimated d-axis is aligned to the $-d$-axis.

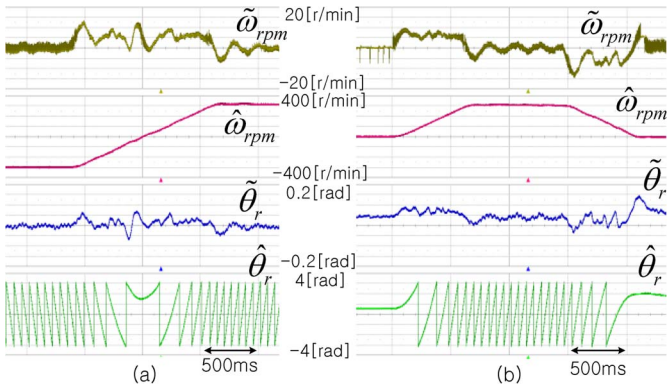

Fig. 13. Proposed sensorless speed control with no load. (a) -300 r/min $\rightarrow$ 300 r/min. (b) 0 r/min $\rightarrow$ 300 r/min $\rightarrow$ 0 r/min.

mentioned in Section III-B, $\hat{\theta}_r = \hat{\theta}_{inj} - \pi/4$. From the test results, (18) can be clearly confirmed. ε_f is negative when $\hat{\theta}_{inj}$ is ahead of θ_{inj}, and ε_f is positive when $\hat{\theta}_{inj}$ is behind of θ_{inj}, so the rotor position can be tracked with a simple error correction controller whose input is ε_f.

Fig. 12 shows the experimental results of an initial $+d$-axis detection. The proposed sensorless method settles down at either $+d$- or $-d$-axes depending on the initial condition. In this experiment, the intended injection angle, i.e., θ_{inj}, is set as zero. The rotor-side inverter controls the dc component of i^r_{dr} to build up the field flux and the high-frequency component of $i^r_{d_{injr}}$ for the power transfer. Meanwhile, during the initial angle detection period, $i^r_{q_{injr}}$ is controlled to make pulses to distinguish the polarity of the d-axis. After initial angle detection, $i^r_{q_{injr}}$ is regulated to null in order to reduce the copper loss. Because $i^{\hat{r}}_{q_{injs}}$ has undesired signal noise, $LPF(i^{\hat{r}}_{q_{injs}})$ is used to distinguish the $+d$- and $-d$-axes. Fig. 12(a) and (b) represents the case when the estimated d-axis is aligned to the $+d$- and $-d$-axes, respectively. By comparing the signs of the peaks, the $+d$-axis can be found with the devised initial $+d$-axis detection method.

Fig. 13 shows the speed control performance of the proposed sensorless method. Speed error $\tilde{\omega}_{rpm}$, estimated speed $\hat{\omega}_{rpm}$, angle error $\tilde{\theta}_r$, and estimated angle $\hat{\theta}_r$ are shown starting from the top. The proposed sensorless controller regulated speed from -300 to 300 r/min with no load condition in Fig. 13(a). During this speed control, the speed error was lower than 15 r/min, whereas the angle error was lower than 0.1 rad, 5.7°, at the peak. The estimated angle varies well according to the variation of the estimated speed. The proposed sensorless controller regulated speed from 0 to 300 r/min and back to 0 r/min at no load condition in Fig. 13(b). During this speed control, the speed error was lower than 15 r/min, and the error information was lower than 0.15 rad, 8.6°, at the peak.

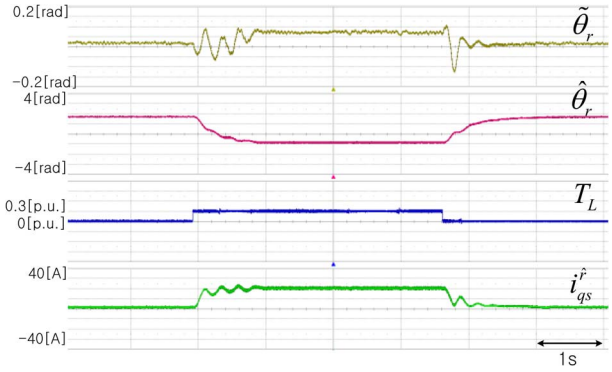

Fig. 14. Step load torque (30% of rated torque) response at standstill speed control.

Fig. 14 shows the load torque response performance of the proposed sensorless method. Angle error $\tilde{\theta}_r$, estimated angle $\hat{\theta}_r$, load torque T_L, and stator-side estimated rotor reference q-axis current $i^{\hat{r}}_{qs}$ are shown starting from the top. The proposed sensorless controller regulated speed as null, whereas 0.3 p.u. of the load torque was applied and removed in a step manner. During this torque response, the angle error was lower than 0.15 rad, 8.6°, at the peak.

V. Conclusion

In this paper, a sensorless control method for SMIIR has been proposed. This method creates a virtual resistance saliency using the rotor-side inverter for the SMIIR, which does not have adequate magnetic saliency for the conventional high-frequency sensorless control. Because this artificially generated virtual saliency is independent of physical saliency, the saliency ratio can be arbitrarily set, and the axes of saliency can be arbitrarily placed.

Based on the proposed virtual resistance saliency, the rotor position information can be extracted from the relationship between the high-frequency stator voltage and current, regardless of the physical machine parameters or operating conditions. Because the SMIIR inherently injects a high-frequency voltage to transfer electric power to the rotor-side inverter, there is no need to inject additional voltage for the high-frequency sensorless control. Moreover, an initial d-axis detection algorithm using the artificial asymmetry of the current response by the rotor-side inverter has been devised.

The proposed method has been verified by an experimental test with the prototype SMIIR. The error information based on the virtual resistance saliency, the initial d-axis detection

algorithm, and the speed control performances under various operating conditions have been verified. The proposed sensorless control method for SMIIR might enhance the applicability of the SMIIR to industrial fields, such as traction machines for road vehicles and generators for conventional and renewable energy systems.

REFERENCES

[1] D. W. Novotny and T. A. Lipo, *Vector Control and Dynamics of AC Drives*. Oxford, U.K.: Clarendon, 1996.

[2] J. Holtz, "Sensorless control of induction machines—with or without signal injection?" *IEEE Trans. Ind. Electron.*, vol. 53, no. 1, pp. 7–30, Feb. 2006.

[3] P. P. Acarnley and J. F. Watson, "Review of position-sensorless operation of brushless permanent-magnet machines," *IEEE Trans. Ind. Electron.*, vol. 53, no. 2, pp. 352–362, Apr. 2006.

[4] S. Ogasawara and H. Akagi, "An approach to position sensorless drive for brushless DC motor," *IEEE Trans. Ind. Appl.*, vol. 27, no. 5, pp. 928–933, Sep./Oct. 1991.

[5] K. D. Hurst, T. G. Habetler, G. Griva, and F. Profumo, "Zero-speed tacholess IM torque control: Simply a matter of stator voltage integration," *IEEE Trans. Ind. Appl.*, vol. 34, no. 4, pp. 790–795, Jul./Aug. 1998.

[6] R. B. Sepe and J. H. Lang, "Real-time observer-based (adaptive) control of a permanent-magnet synchronous motor without mechanical sensors," *IEEE Trans. Ind. Appl.*, vol. 28, no. 6, pp. 1345–1352, Nov./Dec. 1992.

[7] A. B. Kulkarni and M. Ehsani, "A novel position sensor elimination technique for interior permanent-magnet synchronous drive," *IEEE Trans. Ind. Appl.*, vol. 28, no. 1, pp. 144–150, Jan./Feb. 1992.

[8] V. Petrovic, A. M. Stankovic, and V. Blasko, "Position estimation in salient PM synchronous motors based on PWM excitation transients," *IEEE Trans. Ind. Appl.*, vol. 39, no. 3, pp. 835–843, May/Jun. 2003.

[9] M. Mamo, K. Ide, M. Sawamura, and J. Oyama, "Novel rotor position extraction based on Carrier Frequency Component Method (CFCM) using two reference frames for IPM drives," *IEEE Trans. Ind. Electron.*, vol. 52, no. 5, pp. 508–514, Apr. 2005.

[10] S. Ogasawara and H. Akagi, "Implementation and position control performance of a position-sensorless IPM motor drive system based on magnetic saliency," *IEEE Trans. Ind. Appl.*, vol. 34, pp. 806–812, Jul./Aug. 1998.

[11] M. Schroedl, "Sensorless control of AC machine at low speed and standstill based on the 'INFORM' method," in *Conf. Rec. IEEE IAS Annu. Meeting*, 1996, pp. 270–277.

[12] P. L. Jansen and R. D. Lorenz, "Transducerless position and velocity estimation in induction and salient AC machines," *IEEE Trans. Ind. Appl.*, vol. 31, no. 2, pp. 240–247, Mar./Apr. 1995.

[13] S. Kim, Y.-C. Kwon, S.-K. Sul, J. Park, and S.-M. Kim, "Position sensorless operation of IPMSM with near PWM switching frequency signal injection," in *Proc. IEEE 8th ICPE-ECCE Asia*, 2011, pp. 1660–1665.

[14] Y. Jeong, R. D. Lorenz, T. M. Jahns, and S. K. Sul, "Initial rotor position estimation of an interior permanent-magnet synchronous machine using carrier-frequency injection methods," *IEEE Trans. Ind. Appl.*, vol. 41, no. 1, pp. 38–45, Jan./Feb. 2005.

[15] J. H. Jang, S. K. Sul, J. I. Ha, K. Ide, and M. Sawamura, "Sensorless drive of surface-mounted permanent-magnet motor by high-frequency signal injection based on magnetic saliency," *IEEE Trans. Ind. Appl.*, vol. 39, no. 4, pp. 1031–1039, Jul./Aug. 2003.

[16] K. Ide, J. K. Ha, and M. Sawamura, "A hybrid speed estimation of flux observer for induction motor drives," *IEEE Trans. Ind. Electron.*, vol. 53, no. 1, pp. 130–137, Feb. 2006.

[17] M. J. Corley and R. D. Lorenz, "Rotor position and velocity estimation for a salient-pole permanent magnet synchronous machine at standstill and high speeds," *IEEE Trans. Ind. Appl.*, vol. 34, no. 4, pp. 784–789, Jul./Aug. 1998.

[18] R. Leidhold and P. Mutschler, "Improved method for higher dynamics in sensorless position detection," in *Proc. IEEE IECON*, 2008, pp. 1240–1245.

[19] Y.-D. Yoon, S.-K. Sul, S. Morimoto, and K. Ide, "High bandwidth sensorless algorithm for AC machines based on square-wave-type voltage injection," *IEEE Trans. Ind. Appl.*, vol. 47, no. 3, pp. 1361–1370, May/Jun. 2011.

[20] R. Masaki, S. Kaneko, M. Hombu, T. Sawada, and S. Yoshihara, "Development of a position sensorless control system on an electric vehicle driven by a permanent magnet synchronous motor," in *Proc. PCC-Osaka*, 2002, vol. 2, pp. 571–576.

[21] S. Kim, J. I. Ha, and S. K. Sul, "PWM switching frequency signal injection sensorless method in IPMSM," *IEEE Trans. Ind. Appl.*, vol. 48, no. 5, Sep./Oct. 2012.

[22] J. I. Ha, K. Ide, T. Sawa, and S. K. Sul, "Sensorless rotor position estimation of an interior permanent-magnet motor from initial states," *IEEE Trans. Ind. Appl.*, vol. 39, no. 3, pp. 761–767, May/Jun. 2003.

[23] J. I. Ha and S. K. Sul, "Sensorless field-orientation control of an induction machine by high-frequency signal injection," *IEEE Trans. Ind. Appl.*, vol. 35, no. 1, pp. 45–51, Jan./Feb. 1999.

[24] D. D. Reigosa, P. Garcia, F. Birz, D. Raca, and R. D. Lorenz, "Modeling and adaptive decoupling of high-frequency resistance and temperature effects in carrier-based sensorless control of PM synchronous machines," *IEEE Trans. Ind. Appl.*, vol. 46, no. 1, pp. 139–149, Jan./Feb. 2010.

[25] E. Jung, S. Kim, J. I. Ha, and S. K. Sul, "Control of a synchronous motor with an inverter integrated rotor," *IEEE Trans. Ind. Appl.*, vol. 48, no. 6, pp. 1993–2001, Nov./Dec. 2012.

[26] A. Vignaud and H. Fennel, "Efficient electric powertrain with externally excited synchronous machine without rare earth magnets using the example of the result system solution," presented at the Vienna Motor Symposium, Vienna, Austria, 2012. [Online]. Available: http://www.conti-online.com/generator/www/de/de/continental/automotive/general/powertrain/download/2012_wien_vortrag_uv.pdf

Sehwa Choe (S'13) received the B.S. and M.S. degrees in electrical engineering and computer science from Seoul National University, Seoul, Korea, in 2011 and 2013, respectively, where he is currently working toward the Ph.D. degree.

His current research interests include sensorless control of electrical machines and capacitorless inverters.

Eunsoo Jung (S'08) was born in Korea in 1983. He received the B.S. degree in mechanical and aerospace engineering and the Ph.D. degree in electrical engineering from Seoul National University, Seoul, Korea, in 2005 and 2012, respectively.

He is currently a Research Engineer with Doosan Infracore Company Ltd., Seoul. His current research interests include efficient and reliable hybrid systems for construction equipment applications.

Seung-Ki Sul (S'78–M'80–SM'98–F'00) received the B.S., M.S., and Ph.D. degrees in electrical engineering from Seoul National University, Seoul, Korea, in 1980, 1983, and 1986, respectively.

From 1986 to 1988, he was an Associate Researcher with the Department of Electrical and Computer Engineering, University of Wisconsin, Madison, WI, USA. From 1988 to 1990, he was a Principal Research Engineer with Gold Star Industrial Systems Company, Seoul. Since 1991, he has been a member of the Faculty of the School of Electrical Engineering, Seoul National University, where he is currently a Full Professor. From 2003 to 2004, he was a Research Director and an Acting Consultant for Yaskawa Electric Company, Kitakyushu, Japan. From 2005 to 2007, he was the Vice Dean of the Engineering College of Seoul National University. From 2008 to 2011, he was the President of the Electrical Engineering Science Research Institute funded by the Korean Government. He has published over 120 peer-reviewed journal papers, mainly in IEEE TRANSACTIONS. His current research interests include power electronic control of electrical machines, electric/hybrid vehicles and ship drives, and power-converter circuits for renewal energy sources.

Dr. Sul was the Technical Chair of the IEEE PESC 2006 conference and the General Chair of the IEEE ECCE-Asia 2011. He is currently the Editor-in-Chief of the *Journal of Power Electronics*, which is an SCIE-registered journal published by the Korean Power Electronics Institute, Seoul.